# Terahertz Phase Retrieval Imaging in Reflection

**NIKOLAY V. PETROV**[1,*], **JEAN-BAPTISTE PERRAUD**[2], **ADRIEN CHOPARD**[2,3], **JEAN-PAUL GUILLET**[2], **OLGA A. SMOLYANSKAYA**[1], **AND PATRICK MOUNAIX**[2]

[1] *Institute of Photonics and Optical Information Technologies, ITMO University, Kronverkskiy 49, 197101 Saint-Petersburg, Russia*
[2] *IMS Laboratory, University of Bordeaux, UMR CNRS 5218, 351 Cours de la Libération Bâtiment A31, 33405 Talence, France*
[3] *Lytid SAS, 8 rue la Fontaine, 92120 Montrouge, France*
[*] *Corresponding author: n.petrov@niuitmo.ru*

**Terahertz phase retrieval is a promising technique able to assess the complex diffracted wave properties through an iterative processing algorithm. In this letter, we demonstrate the implementation of this technique in reflection geometry with a continuous wave acquisition system working at 0.287 THz. To ensure a high signal-to-noise ratio in the measured dataset, we proposed a double parallel recording scheme with one detector and two lock-in amplification operating with the complimentary sensitivity setting. This provided a higher numerical aperture than conventional raster-scanning focal plane imaging. A specialized digital interferometric post-processing procedure was applied to obtain a surface heights map from the reconstructed phase distribution in the object's irradiated area.** © 2020 Optical Society of America

Terahertz (THz) holographic imaging is a prospective approach to lensless visualization that is of great interest thanks to the simplicity of its experimental setup, the ability of numerical image reconstruction in post-processing mode, as well as high achievable resolution. Being one of the last mastered frequency ranges of the electromagnetic spectrum, the THz band presents great opportunities for the introduction of modern imaging approaches that have been demonstrated in other spectral regions. As discussed in [1], the various source types, with fundamental generation differences between pulsed broadband terahertz radiation and continuous wave (CW), influence on the possibilities of technical implementation of the imaging techniques. THz holographic imaging, operating at fixed-frequency with CW sources, provides no spectral information, but utilizes simple, compact and cost-effective equipment. Similarly to the visible range of the electromagnetic spectrum, terahertz digital holography and phase retrieval from intensity distributions can be applied to achieve phase imaging. Contrary to off-axis holography, phase retrieval stands more efficiently in terms of space-bandwidth product to provide a higher spatial resolution [2]. Moreover, due to the single-beam mode, it requires lower power of THz sources and remains more compact.

The first work in this field was off-axis holography, implemented in a transmission mode as a proof-of-concept by Mahon et al. in 2006 [3]. Quite a lot of preliminary work on phase retrieval had been done [4–7] before any application-oriented experimental results were obtained [8, 9]. These days, due to more efficient emitters and detection systems, a growing body of research have been observed in this field [10–12]. Basically, relatively flat objects are being investigated, and the focus on practical applications of these studies is remaining sparse. The main experimental works on this topic deal with twin image suppression in inline holography layout [13–15], autofocusing [16] and resolution enhancement [17]. The real-time holographic recording in transmission mode required for practical use was demonstrated in 2011 by Choporova et al., using a free-electron laser as a generator [18]. In continuation of the effort in this field, off-axis THz holography in reflection mode was demonstrated in 2015 [19]. A few months later, Locatelli et al. published similar work oriented to applied tasks [20]. As for submillimeter CW in-line holography, it was also implemented for amplitude imaging [21], while single beam phase retrieval imaging in reflection in this frequency range has not been demonstrated yet.

In this paper, we present THz phase retrieval from diffracted intensity distributions acquired in the reflection mode. To increase the signal-to-noise ratio under the conditions of weak reflection of the incident radiation from the surface of the object, we have directed the signal from one detector onto two lock-in amplifiers (LIA) with complementary sensitivity settings to obtain recorded intensity distributions with high dynamic range. As the phase retrieval technique, single-beam multiple-intensity reconstruction (SBMIR) algorithm was used since it offers a fast iterative phase recovery convergence through a simplified setup implementation (see Fig. 1). It is based on the processing of diffracted intensity distributions set $I_z(x, y)$, which has been successively recorded at different distances $z_j$ from the investigated object. This algorithm has been successfully demonstrated in transmission [22], diffuse transmission and reflection [23] configuration in the visible range of electromagnetic spectrum, while only the transmission scheme has been investigated in the THz frequency range [24].

Figure 1 provides a descriptive scheme of the implemented experimental setup for recording intensity distributions set for THz phase retrieval in a reflection configuration. A Gunn diode with frequency multiplication chain, emitting at a frequency of $\nu = 0.287$ THz (wavelength $\lambda = 1044.57$ $\mu$m) with a power of 14
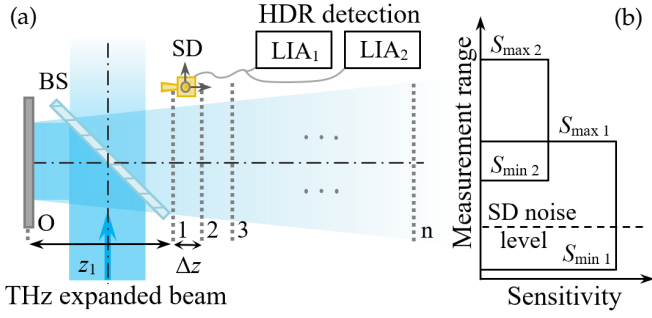
**Fig. 1.** A diagram of the experimental implementation for phase retrieval measurement in reflection configuration, using high dynamic range (HDR) detection (a), HDR sensitivity setting diagram for detection (b).

mW, was used in conjunction with a Schottky diode detector (SD, integrated single-pixel detector without antenna horn with 71 dB dynamic range). We characterized the beam profile to verify that it was collimated to a suitable area of about $8 \times 8$ cm$^2$. Via reflection from a 45° beam splitter (BS), the static object (O) was illuminated by an extended collimated beam. While after reflection from the object and transmission through the BS, the diffracted field was recorded by acquiring a sequence of images at multiple distances along the $z$ axis through a raster scanning pattern. A metallic shuriken was used as the test reflective object. The illuminated area of the object in the phase retrieval experiment contained several concave Chinese characters, including the king kanji 王.

The successive reflected intensity profiles from the object $I_z(x,y)$ were captured at axially spaced n = 27 planes (typically for such implementations n = 20 – 30) with constant separation of $\Delta z = 5$ mm, the first of which was located at a distance $z_0 = 83$ mm from the object plane due to the BS induced obstruction. A 8 cm diameter for the probing beam was achieved due to a beam expanding setup and the $240 \times 240$ pixel images with a pitch $\Delta x = \Delta y = 0.5$ mm ($\approx 0.5\lambda$) were recorded by the SD during the time-consuming 3D raster scanning with a total measurement time close to 36 hours.

In comparison with a transmission geometry, the presence of a beam splitter on the path of the reflected wavefront imposes a restriction on the minimum permissible distance for recording data between the object and the first measurement plane ($n = 1$ in Fig. 1), thereby making the detection of high spatial frequencies difficult. The beam splitter also induces ineluctable power losses, which exacerbates the main challenge of the practical demonstration of THz phase retrieval in the reflection mode, namely the recording of a weak signal with both limited source emission power and detector sensitivity. Such diffractive measurements display large disparities in the intensity distribution of the reflected beam, depending on the position and distance of the detector in regard to the object. A large measurement dynamic range is then required. In this experiment, the output emitter beam was mechanically modulated using a rotating chopper at 235 Hz, and the SD was connected to lock-in amplifiers (LIAs). Commonly, the use of a single LIA leads to a limited dynamic range, usually 30 dB [25], due to intrinsic LIA hardware limitations. To overcome these limitations, two distinct LIAs with complementary sensitivity settings have been connected with the SD for high dynamic range (HDR) detection. Data merging, using the lower sensitivity LIA$_2$ setting in the

case of saturation, and the high sensitivity LIA$_1$ setting in the case of weak signal levels, was employed to reach an adequate merged dynamic range of 50 dB, limited by the detectors noise level and source emission power.

Let us denote the signal to be digitized as $S$, while $S_1$ and $S_2$ are its corresponding values after the digitizing with LIA$_1$ and LIA$_2$, such that $S_{\min 1} < S_1 < S_{\max 1}$ and $S_{\min 2} < S_2 < S_{\max 2}$. Complementary LIA sensitivity settings are chosen so that $S_{\max 1} \gtrsim S_{\min 2}$. Then, as displayed on Fig. 1 (b), for each n measurement plane $(x,y)$ we have:

$$I_n(x,y) = \begin{cases} S_{1n}(x,y) & \text{if} \quad S < \Gamma \cdot S_{\max 1}, \\ S_{2n}(x,y) & \text{otherwise} \quad (S \leq S_{\max 2}). \end{cases} \quad (1)$$

Here $\Gamma$ is a regulation factor, which is set to 0.75 for our implementation to avoid data mismatch of LIA's dynamic range extremities. Figure 2 displays an example of the recorded intensity distributions sets: $S_{1n}$ and $S_{2n}$ with the voltage of LIA$_1$ and LIA$_2$ fixed at 20 mV and 500 mV, respectively in left and center. The resulting HDR images $I_n(x,y)$ are shown in the right.
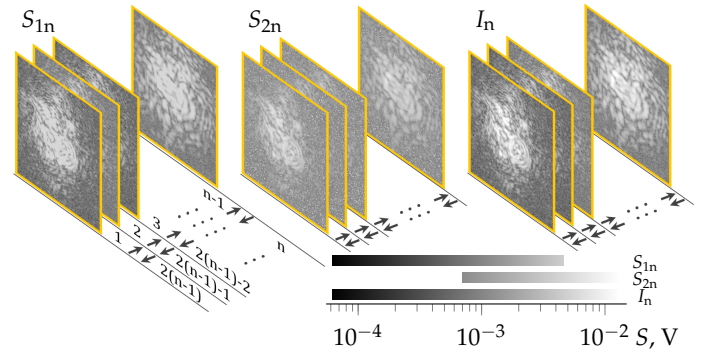


**Fig. 2.** An example of recorded intensity distribution sets in the logarithmic colormap: recorded by LIA$_1$ ($S_{1n}$), LIA$_2$ ($S_{2n}$) and synthesized HDR images ($I_n$). The arrows denote the sequence of propagation based on SBMIR algorithm.

The SBMIR algorithm is based on the numerical solution of the angular spectrum equation for beam propagation in the free space, which defines the evolution of the diffractive transform of the wave front $U_2(x,y)$ between measurement planes:

$$U_2(x,y) = \mathcal{F}^{-1}\{H(f_x, f_y, z) \cdot \mathcal{F}[U_1(x,y)]\}, \quad (2)$$

with the free space propagation transfer function $H(f_x, f_y, z)$:

$$H(f_x, f_y, z) = \begin{cases} e^{i\frac{2\pi}{\lambda}z\sqrt{1-\lambda^2(f_x^2+f_y^2)}} & \text{if } f_x^2 + f_y^2 \leq \frac{1}{\lambda^2}; \\ e^{-\frac{2\pi}{\lambda}z\sqrt{1-\lambda^2(f_x^2+f_y^2)}} & \text{if } f_x^2 + f_y^2 > \frac{1}{\lambda^2}. \end{cases} \quad (3)$$

Here $U_1(x,y)$ is the field at the source plane, $U_2(x,y)$ is the field at the observation plane, $\lambda$ is the wavelength, $z$ is the distance between the propagation planes, $\mathcal{F}$ and $\mathcal{F}^{-1}$ are operators of direct and inverse Fourier transform, $(x,y)$ and $(f_x, f_y)$ are the coordinates in spatial and frequency domains, respectively.

As demonstrated in Fig. 2, from the recorded intensity distribution set, the field reconstruction, based on Eqs. (2 – 3), is performed as follows: the initial wavefront estimation in the first measurement plane is constructed from the square root from the first intensity measurement and plane phase. Constructed wavefront estimation is propagated in the forward direction toward the second measured plane where the estimated phase is

kept, while the amplitude is replaced by the square root from the second measured intensity distribution. In a similar way, this new wavefront estimation is propagated in the forward direction, and the same actions are repeated for each measurement plane. Reaching the last measurement plane, this sequence is repeated in backward direction. Thus, one iteration encloses $2(n-1)$ propagation steps. At the end of each iteration, reconstructed amplitude and phase images in the object plane can be visualized to validate the algorithm convergence.
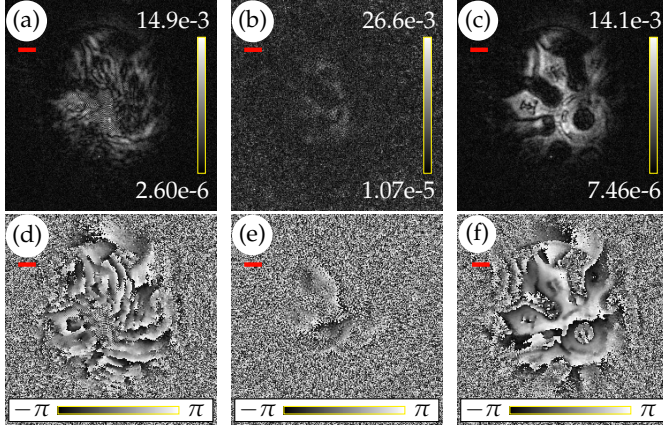


**Fig. 3.** Typical reconstructed amplitude (top row) and phase (bottom row) distributions from the data sets recorded by $LIA_1$ (a, d), $LIA_2$ (b, e) and HDR (c, f) measurement data sets. Red lines are the 10 mm scale bar.

Figure 3 shows the reconstructed amplitude and phase profiles of the field in the object plane obtained from the data sets, which were previously shown in Fig. 2. Note that the amplitude values range (in a.u.) inherits the signal's measurement range (in V.), shown in Fig 2. Due to the high sensitivity setting of $LIA_1$, the resulting data set (Fig. 2 (a)) contains low-intensity high spatial-frequency components, but suffers from oversaturation in the central region. As a result, due to the lack of information from the diffraction patterns center, the SBMIR algorithm does not converge toward an acceptable field with this saturated input data set (Fig. 3 (a, d)). Figure 3 (c, f) reveals the high resolution of the reconstructed wavefront achieved due to the high dynamic range data set used in the SBMIR algorithm. Indeed, the dynamic range is the main limiting factor for such diffraction measurement since the achieved resolution is limited by the capabilities of recording of low-intensity high spatial frequencies. Beside the high-resolution amplitude reconstruction (Fig. 3 (c)), the HDR phase reconstruction, shown in Fig. 3 (f), depicts a slight tilt of the object relative to the imaging planes. The topological profile of the object can as well be noticed in the phase reconstruction. As a highlight for the prevalence of this HDR measurement technique, the self-explanatory reconstructed amplitude profiles are displayed using an improved HDR measurement scheme and classical single LIA detection with dynamic ranges 50 and 30 dB, correspondingly. The signal from $LIA_2$ in the dynamic range restricted by 30 dB clearly demonstrates a lack of sensitivity (Fig. 2 (b)). The high noise level in the measurement data set limits the detection of low signals, thus making the detection of high spatial frequencies impossible due to their low amplitudes. As demonstrated in Fig. 3 (b, e), compared to HDR case in Fig. 3 (c, f), $LIA_2$ dynamic range ensures no successful wavefront reconstruction.
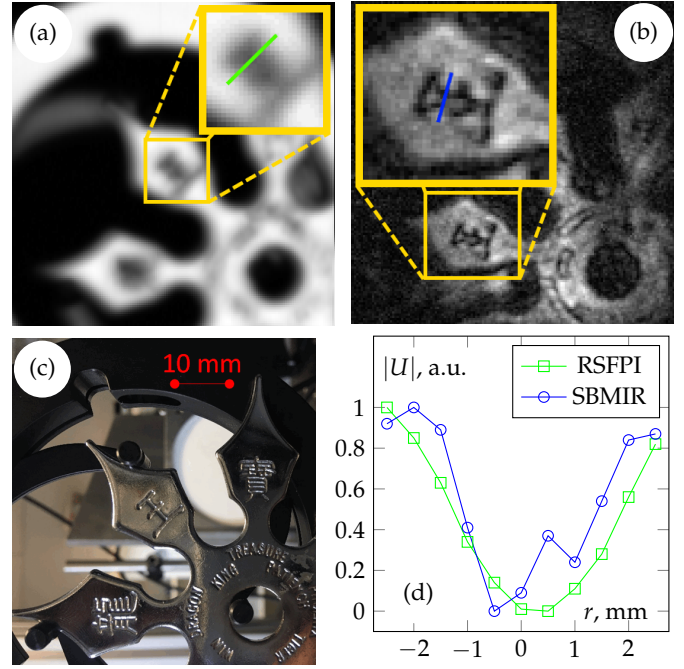


**Fig. 4.** Amplitude distributions of the considered sample obtained by a RSFPI at 0.287 THz with $NA = 0.25$ (a) and by SBMIR (b), enlarged amplitude reconstruction resulting from SBMIR algorithm on HDR diffractive measurement set, (c) photo of the object illuminated by visible EM range, (d) cross-sections, plotted through the corresponding green and blue lines on the image of the Chinese character, shown at the insets of (a) and (b).

HDR phase retrieval imaging is more practical than raster-scanning focal plane imaging (RSFPI) due to the inherent lensless ability to provide a high numerical aperture. For the first measurement plane, we estimated $NA = 0.72$, while for conventional RSFPI it typically $1.5 - 3$ times less. Fig. 4 displays a plain illustrative comparison of the results obtained by both techniques.

To obtain a quantitative height map from the reconstructed reflected object wavefront, the following 8-step procedure was applied: (i) Based on the amplitude image, a binary mask was manually created for the contouring of the object. It should be noted that the mask boundaries were slightly smaller than the irradiated surface area of the shuriken since its rounded edges allow no sufficient amplitude reconstruction. (ii) This mask was superimposed on the phase image to eliminate the phase noise inherent to undetermined amplitude spatial areas. (iii) The wavefront was oversampled to subsequently undergo tilt correction by digital interferometric processing with synthesized hologram, as described in [26]. Technically, each wavefront pixel was divided into 64 identical elements, thus providing an 8-fold increase in grid elements for each coordinate, and was then multiplied with an inclined plane reference phase term $\exp(ik/\lambda(x\cos\beta_x) + y\cos\beta_y)$, where the angle $\beta = (\beta_x, \beta_y)$ is determined so that each fringe spacing matches 8 pixels. Thus, synthetic off-axis hologram with maximum fringe contrast is simulated (Fig. 5 (a)). (iv) The phase distribution is then recovered from the hologram using a slightly different angle, which provided correction of the general surface tilt of the shuriken (Fig. 5 (b)). (v) The background phase (Fig. 5 (c)) is then sub-

tracted. This background phase was retrieved by SBMIR from preliminarily recorded diffraction patterns of a reference mirror with a small reflective bead in front of it, introducing a perturbation in the incident field. The bead phase perturbation has been concealed by a phase averaging over the neighboring values. (vi) The resulting object area phase was then unwrapped and (vii) rescaled to its original ($1\times$) size. (viii) The height map (Fig. 5 (d)) is then obtained as $h(x, y) = (\lambda/4\pi)\varphi(x, y)$. It displays good agreement with the measurements of topological features conducted by optical microscopy: the 275 $\mu$m reference depth in the $\mp$ cross-section schematically shown in Fig. 5 (e)).
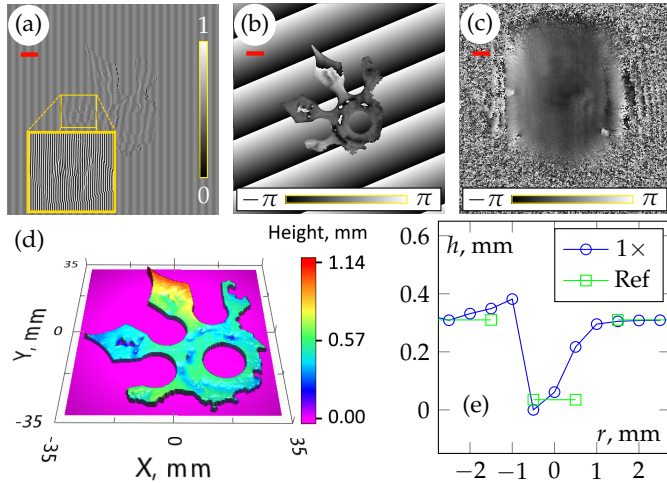


**Fig. 5.** Details of numerical post-processing of reconstructed phase. Synthesized off-axis hologram (a), reconstructed phase with tilt correction (b), reconstructed background phase after central area patching (c), reconstructed surface map (d) and (e) phase cross-section through the same path as in Fig. 4 (b, d). Red lines are the 10 mm scale bar.

For further optimization of this measurement technique, a solution can consist in increasing the total available reflected energy by removing the beam splitter. Such an improvement can be implemented through the illumination of the reflective object under a non-normal beam incidence and the orientation of the measurement system at the maximum angle of reflection. In terms of algorithm, this evolution can require the inclusion of additional processing steps to compensate the tilt between the object plane and the measurement planes as well as the implementation of geometrical transformations to correct the projection induced shrinkage of the reconstructed amplitude and phase images. Such developments have been performed in classical reflective holography with a reference beam [19]. The use of a matrix detector can also increase energy efficiency by reducing the beam size, without sacrificing acquisition time.

In conclusion, THz phase retrieval with single-beam multiple intensity reconstruction (SBMIR) algorithm was demonstrated for the first time in the reflection mode using millimeter waves at the frequency of 0.287 THz. The synthesis of high-dynamic-range intensity distributions from a single detector with two independent lock-in amplifiers was proposed and experimentally validated, that resulted in drastic field reconstructions improvement. We believe, such a solution may be extremely useful also in other related imaging applications as well. The advantages of such a proposed approach were demonstrated in the experiments with the increase of dynamic range of the measured intensity distributions from 30 to 50 dB, in comparison with single lock-in detection and reference widespread technique of RSFPI at the same frequency. It was established that, in such optimized configurations, SBMIR THz phase retrieval provides improved resolution in the amplitude images to reach submillimeter resolution as well as reliable phase distributions reconstructions eligible for quantitative topological measurements.

**Disclosures.** The authors declare no conflicts of interest.

## REFERENCES

1. N. Karpowicz, H. Zhong, J. Xu, K.-i. Lin, J.-S. Hwang, and X.-C. Zhang, Semicond. Sci. Technol. **20**, S293 (2005).
2. I. A. Shevkunov, N. S. Balbekin, and N. V. Petrov, Proc. SPIE **9271**, 927128 (2014).
3. R. J. Mahon, J. A. Murphy, and W. Lanigan, Opt. Comm. **260**, 469 (2006).
4. G. Hislop, G. C. James, and A. Hellicar, IEEE Trans. Antennas Propag. **55**, 2332 (2007).
5. G. Hislop, L. Li, and A. Hellicar, IEEE Trans. Antennas Propag. **57**, 286 (2009).
6. N. V. Petrov, A. N. Galiaskarov, T. Y. Nikolaeva, and V. G. Bespalov, Proc. SPIE **8413**, 84131T (2012).
7. N. V. Petrov, A. A. Gorodetsky, and V. G. Bespalov, Proc. SPIE **8846**, 88460S (2013).
8. L. Rong, T. Latychevskaia, D. Wang, X. Zhou, H. Huang, Z. Li, and Y. Wang, Opt. Express **22**, 17236 (2014).
9. L. Rong, T. Latychevskaia, C. Chen, D. Wang, Z. Yu, X. Zhou, Z. Li, H. Huang, Y. Wang, and Z. Zhou, Sci. Rep. **5** (2015).
10. L. Valzania, T. Feurer, P. Zolliker, and E. Hack, Opt. Lett. **43**, 543 (2018).
11. Z. Li, R. Zou, W. Kong, X. Wang, Q. Deng, Q. Yan, Y. Qin, W. Wu, and X. Zhou, Photonics Res. **7**, 1391 (2019).
12. D. Wang, B. Li, L. Rong, F. Tan, J. J. Healy, J. Zhao, and Y. Wang, Opt. Lett. **45**, 1391 (2020).
13. L. R. Lu Rong, F. P. Feng Pan, W. X. Wen Xiao, Y. L. Yan Li, and F. W. Fanjing Wang, Chin. Opt. Lett. **10**, 060902 (2012).
14. L. Rong, Y. Li, S. Liu, W. Xiao, F. Pan, and D. Wang, Opt. Lasers Eng. **51**, 553 (2013).
15. J. Hu, Q. Li, and S. Cui, Appl. Opt. **53**, 7112 (2014).
16. H. Huang, D. Wang, L. Rong, X. Zhou, Z. Li, and Y. Wang, Opt. Comm. **346**, 93 (2015).
17. Z. Li, L. Li, Y. Qin, G. Li, D. Wang, and X. Zhou, Opt. Express **24**, 21134 (2016).
18. Y. Y. Choporova, M. Vlasenko, V. Gerasimov, T. Irgalin, B. Knyazev, and V. Cherkassky, Radiophys. Quant. El.+ **54**, 585 (2012).
19. P. Zolliker and E. Hack, Opt. Express **23**, 10957 (2015).
20. M. Locatelli, M. Ravaro, S. Bartalini, L. Consolino, M. S. Vitiello, R. Cicchi, F. Pavone, and P. De Natale, Sci. Rep. **5**, 13566 (2015).
21. X. Gao, C. Li, and G.-Y. Fang, Chin. Opt. Lett. **30**, 068401 (2013).
22. G. Pedrini, W. Osten, and Y. Zhang, Opt. Lett. **30**, 833 (2005).
23. P. Almoro, G. Pedrini, and W. Osten, Appl. Opt. **45**, 8596 (2006).
24. L. Valzania, P. Zolliker, and E. Hack, Optica. **6**, 518 (2019).
25. R. User's Manual Model SR844, Inc., Sunnyvale, CA (1997).
26. A. Belashov, N. Petrov, and I. Semenova, Opt. Express **22**, 28363 (2014).

## FULL REFERENCES

1.  N. Karpowicz, H. Zhong, J. Xu, K.-i. Lin, J.-S. Hwang, and X.-C. Zhang, "Comparison between pulsed terahertz time-domain imaging and continuous wave terahertz imaging," Semicond. Sci. Technol. **20**, S293–S299 (2005).

2.  I. A. Shevkunov, N. S. Balbekin, and N. V. Petrov, "Comparison of digital holography and iterative phase retrieval methods for wavefront reconstruction," Proc. SPIE **9271**, 927128 (2014).

3.  R. J. Mahon, J. A. Murphy, and W. Lanigan, "Digital holography at millimetre wavelengths," Opt. Comm. **260**, 469–473 (2006).

4.  G. Hislop, G. C. James, and A. Hellicar, "Phase Retrieval of Scattered Fields," IEEE Trans. Antennas Propag. **55**, 2332–2341 (2007).

5.  G. Hislop, L. Li, and A. Hellicar, "Phase Retrieval for Millimeter- and Submillimeter-Wave Imaging," IEEE Trans. Antennas Propag. **57**, 286–290 (2009).

6.  N. V. Petrov, A. N. Galiaskarov, T. Y. Nikolaeva, and V. G. Bespalov, "The features of optimization of a phase retrieval technique in THz frequency range," Proc. SPIE **8413**, 84131T (2012).

7.  N. V. Petrov, A. A. Gorodetsky, and V. G. Bespalov, "Holography and phase retrieval in terahertz imaging," Proc. SPIE **8846**, 88460S (2013).

8.  L. Rong, T. Latychevskaia, D. Wang, X. Zhou, H. Huang, Z. Li, and Y. Wang, "Terahertz in-line digital holography of dragonfly hindwing: amplitude and phase reconstruction at enhanced resolution by extrapolation," Opt. Express **22**, 17236 (2014).

9.  L. Rong, T. Latychevskaia, C. Chen, D. Wang, Z. Yu, X. Zhou, Z. Li, H. Huang, Y. Wang, and Z. Zhou, "Terahertz in-line digital holography of human hepatocellular carcinoma tissue," Sci. Rep. **5** (2015).

10. L. Valzania, T. Feurer, P. Zolliker, and E. Hack, "Terahertz ptychography," Opt. Lett. **43**, 543 (2018).

11. Z. Li, R. Zou, W. Kong, X. Wang, Q. Deng, Q. Yan, Y. Qin, W. Wu, and X. Zhou, "Terahertz synthetic aperture in-line holography with intensity correction and sparsity autofocusing reconstruction," Photonics Res. **7**, 1391 (2019).

12. D. Wang, B. Li, L. Rong, F. Tan, J. J. Healy, J. Zhao, and Y. Wang, "Multi-layered full-field phase imaging using continuous-wave terahertz ptychography," Opt. Lett. **45**, 1391 (2020).

13. L. R. Lu Rong, F. P. Feng Pan, W. X. Wen Xiao, Y. L. Yan Li, and F. W. Fanjing Wang, "Twin image elimination from two in-line holograms via phase retrieval," Chin. Opt. Lett. **10**, 060902–60904 (2012).

14. L. Rong, Y. Li, S. Liu, W. Xiao, F. Pan, and D. Wang, "Iterative solution to twin image problem in in-line digital holography," Opt. Lasers Eng. **51**, 553–559 (2013).

15. J. Hu, Q. Li, and S. Cui, "Research on object-plane constraints and hologram expansion in phase retrieval algorithms for continuous-wave terahertz inline digital holography reconstruction," Appl. Opt. **53**, 7112 (2014).

16. H. Huang, D. Wang, L. Rong, X. Zhou, Z. Li, and Y. Wang, "Application of autofocusing methods in continuous-wave terahertz in-line digital holography," Opt. Comm. **346**, 93–98 (2015).

17. Z. Li, L. Li, Y. Qin, G. Li, D. Wang, and X. Zhou, "Resolution and quality enhancement in terahertz in-line holography by sub-pixel sampling with double-distance reconstruction," Opt. Express **24**, 21134 (2016).

18. Y. Y. Choporova, M. Vlasenko, V. Gerasimov, T. Irgalin, B. Knyazev, and V. Cherkassky, "Recording and reconstruction of in-line holograms of amplitude objects in the terahertz frequency range using a free electron laser," Radiophys. Quant. El.+ **54**, 585–590 (2012).

19. P. Zolliker and E. Hack, "Thz holography in reflection using a high resolution microbolometer array," Opt. Express **23**, 10957–10967 (2015).

20. M. Locatelli, M. Ravaro, S. Bartalini, L. Consolino, M. S. Vitiello, R. Cicchi, F. Pavone, and P. De Natale, "Real-time terahertz digital holography with a quantum cascade laser," Sci. Rep. **5**, 13566 (2015).

21. X. Gao, C. Li, and G.-Y. Fang, "The Realization of Terahertz Image Reconstruction with High Resolution Based on the Amplitude of the Echoed Wave by using the Phase Retrieval Algorithm," Chin. Opt. Lett. **30**, 068401 (2013).

22. G. Pedrini, W. Osten, and Y. Zhang, "Wave-front reconstruction from a sequence of interferograms recorded at different planes," Opt. Lett. **30**, 833–835 (2005).

23. P. Almoro, G. Pedrini, and W. Osten, "Complete wavefront reconstruction using sequential intensity measurements of a volume speckle field," Appl. Opt. **45**, 8596 (2006).

24. L. Valzania, P. Zolliker, and E. Hack, "Coherent reconstruction of a textile and a hidden object with terahertz radiation," Optica. **6**, 518–523 (2019).

25. R. User's Manual Model SR844, "Lock-in amplifier standford research systems," Inc., Sunnyvale, CA (1997).

26. A. Belashov, N. Petrov, and I. Semenova, "Digital off-axis holographic interferometry with simulated wavefront," Opt. Express **22**, 28363–28376 (2014).